Transmon-qubit readout using an *in situ* bifurcation amplification in the mesoscopic regime

R. Dassonneville,[1,2,*] T. Ramos,[3] V. Milchakov,[1] C. Mori,[1] L. Planat,[1] F. Foroughi,[1] C. Naud,[1] W. Hasch-Guichard,[1] J.J. García-Ripoll,[3] N. Roch,[1] and O. Buisson[1]

[1] *Université Grenoble-Alpes, CNRS, Grenoble INP, Institut Néel, Grenoble 38000, France*
[2] *Aix Marseille Université, CNRS, IM2NP, Marseille, France*
[3] *Institute of Fundamental Physics, IFF-CSIC, Calle Serrano 113b, Madrid 28006, Spain*

(Received 31 July 2023; accepted 26 September 2023; published 19 October 2023)

We demonstrate a transmon-qubit readout based on the nonlinear response to a drive of polaritonic meters *in situ* coupled to the qubit. Inside a three-dimensional readout cavity, we place a transmon molecule consisting of a transmon qubit and an ancilla mode interacting via nonperturbative cross-Kerr-coupling. The cavity couples strongly only to the ancilla mode, leading to hybridized lower and upper polaritonic meters. Both polaritons are anharmonic and dissipative, as they inherit a self-Kerr nonlinearity U from the ancilla and effective decay κ from the open cavity. Via the ancilla, the polariton meters also inherit the nonperturbative cross-Kerr-coupling to the qubit. This results in a high qubit-dependent displacement $2\chi > \kappa, U$ that can be read out via the cavity without causing Purcell decay. Moreover, the polariton meters, being nonlinear resonators, present bistability, and bifurcation behavior when the probing power increases. In this work, we focus on the bifurcation at low power in the few-photon regime, called the mesoscopic regime, which is accessible when the self-Kerr and decay rates of the polariton meter are similar, $U \sim \kappa$. Capitalizing on a latching mechanism by bifurcation, the readout is sensitive to transmon-qubit relaxation error only in the first tens of nanoseconds. We thus report a single-shot fidelity of 98.6% while having an integration time of 500 ns and no requirement for an external quantum-limited amplifier.

DOI: 10.1103/PhysRevApplied.20.044050

I. INTRODUCTION

Qubit-state readout is a mandatory step in quantum information processing. For superconducting circuits, dispersive readout is the standard scheme [1,2]. It relies on the transverse interaction between an anharmonic mode, whose first two levels are used as a qubit, and another mode, usually harmonic, used as a meter [3,4]. This transverse interaction couples the qubit polarization to the meter field quadrature and hybridizes the qubit with the meter. In perturbation theory, the resulting dispersive interaction (or perturbative cross-Kerr-coupling) corresponds in first order to an energy-energy interaction where the qubit state shifts the meter frequency and, reciprocally, the number of photons in the meter shifts the qubit frequency. When applying a coherent pulse close to the meter frequency for a time smaller than the relaxation time of the qubit T_1, the qubit state is inferred by distinguishing, in phase space of the acquired output field, the two pointer states of the meter corresponding to the qubit excited or ground states.

Using this dispersive readout, single-shot readout with high fidelity is nowadays routinely achieved, notably thanks to the quantum-limited Josephson parametric amplifier (JPA) [5]. However, the dispersive interaction contains intrinsic limitations, due to the higher-order corrections in perturbation theory. The qubit states are slightly dressed by the meter states, which leads to Purcell decay [6] and prevents an ideal quantum nondemolition (QND) readout [7,8]. In addition, unwanted effects for the readout, such as relaxation and excitation rate of the qubit, can increase with readout photon number $\overline{n}$ [9–13].

To overcome these limitations, a nonperturbative cross-Kerr-coupling between the qubit and the meter has been proposed [14,15] and demonstrated thanks to the property of a transmon molecule [16–19] achieving high fidelity and QND single-shot readout of a transmon qubit [19]. This result was realized through a polariton meter in its linear regime, whose signal was amplified through an external JPA.

Alternatively to JPA, superconducting qubit readout can also be performed using a Josephson bifurcation amplifier (JBA) [20–22]. The JBA is a nonlinear pumped resonator such as the JPA, but it is pumped at a different working

*remy.dassonneville@univ-amu.fr

point, where it presents a nonlinear amplification relationship between its input amplitude and output amplitude, leading to two stable states of small and large output amplitude for input signal below and above the bifurcation threshold, respectively. The information on the qubit state is then encoded into those two output states. In addition, the bifurcation presents hysteresis, leading to a latching readout. The JBA dynamics is controlled by the detuning between the nonlinear resonator and the pump, the resonator losses κ, and its anharmonicity U. A same-chip implementation allows a direct coupling between the qubit and the JBA, with an *in situ* amplifying bifurcation, greatly increasing the quantum detection efficiency [20,22–27]. Here, we propose a readout based on bifurcation amplification of the *in situ* nonlinear polariton meter.

Up to now, bifurcation readout has been realized in the weak anharmonicity limit $U \ll \kappa$ in which the bistability regime is achieved when the photon number $\overline{n}$ in the nonlinear resonator exceeds the critical number $N_{\text{crit}} = \kappa/(3\sqrt{3}U) \gg 1$ [28,29]. However, this large photon number, needed to reach bistability and thus bifurcation, exposes the qubit to excess backaction of the nonlinear cavity [28–32] like inducing qubit-state transitions and thus rendering the readout not QND. Instead of the usual classical regime of weak anharmonicity and large photon number ($U \ll \kappa$, $N_{\text{crit}} \gg 1$), the excess backaction on the qubit could be weakened in the mesoscopic regime ($U \sim \kappa$, $N_{\text{crit}} \sim 1$) where bistability appears with photon number close to unity, $\overline{n} \gtrsim N_{\text{crit}} \sim 1$. This little-explored regime is in between the classical regime and the quantum regime ($U \gg \kappa$, $N_{\text{crit}} \ll 1$), where the system behaves as an effective quantum few-level system [33–35].

In this paper, we demonstrate a transmon-qubit-state latching readout using an *in situ* bifurcation of a polariton resonator in the mesoscopic regime. The polaritons are superpositions of the harmonic cavity mode and the anharmonic ancillary mode of the transmon molecule. They result from the strong coupling and hybridization between them. Both polariton modes inherit the nonlinearity of the ancilla mode, so they effectively behave as two nonlinear Kerr resonators exhibiting bistability [36–39]. By adjusting the ancilla frequency through an external magnetic flux, we control the hybridization and, consequently, the anharmonicity and dissipation of each polariton.

In Sec. II, we discuss details of the transmon molecule, the ancilla-cavity hybridization, the resulting polariton modes, and their tunability. Contrary to our previous work [19], where we considered the linear regime with $\overline{n} \ll N_{\text{crit}}$ and $N_{\text{crit}} \gg 1$, here we investigate the nonlinear regime of the polaritons at large occupation $\overline{n} \gtrsim N_{\text{crit}} \sim 1$. The polariton's response to a strong drive and its dependence on the qubit state are detailed in Sec. III. The hysteretic bistability behavior of the nonlinear upper polaritonic meter is analyzed in Sec. IV. Finally, in Sec. V, we take advantage of this bistability to perform a latching readout of the qubit state with a high single-shot fidelity and without any external quantum-limited amplifier.

II. TUNING THE ANCILLA-CAVITY HYBRIDIZATION

A. Transmon molecule in a cavity

We use the same sample as in Ref. [19]. It consists of a three-dimensional (3D) cavity containing a transmon molecule which is made by coupling inductively and capacitively two nominally identical transmons [16,19] [see Fig. 1(a) and Appendix A]. The device has three modes of interest, namely, the harmonic TE_{101} mode $\hat{c}$ of the rectangular 3D copper cavity with frequency $\omega_c/2\pi = 7.169$ GHz, and the two orthogonal modes of the transmon molecule (for more details see Appendix B and Ref. [19]): (i) a qubit mode, with parameters of standard transmons, protected from interaction with the 3D cavity mode thanks to its symmetric profile, and (ii) an ancilla mode, with weak ($\sim$ MHz) anharmonicity and strong interaction to the cavity g_{ac} due to its antisymmetric mode profile. Indeed, the cavity electrical field is aligned with the field of the ancilla mode while being orthogonal to the field of the qubit mode.

The ancilla is approximated as a weakly nonlinear mode $\hat{a}$ with frequency ω_a tunable by magnetic flux and self-Kerr rate U_a. Moreover, approximating the multilevel transmon as a qubit $\hat{\sigma}_z$, the total system Hamiltonian including cavity, ancilla, and qubit reads

$$\frac{\hat{H}}{\hbar} = \frac{\omega_q}{2}\hat{\sigma}_z + \omega_a\hat{a}^\dagger\hat{a} + \omega_c\hat{c}^\dagger\hat{c} - \frac{U_a}{2}\hat{a}^{\dagger 2}\hat{a}^2 - g_{zz}\hat{\sigma}_z\hat{a}^\dagger\hat{a} + g_{ac}(\hat{c}^\dagger\hat{a} + \hat{a}^\dagger\hat{c}). \tag{1}$$

The qubit $\hat{\sigma}_z$ with frequency $\omega_q/2\pi = 6.283$ GHz and coherence times $T_2, T_1 \simeq 3$ μs is coupled to the ancilla mode $\hat{a}$ via a *nonperturbative* cross-Kerr-coupling with rate g_{zz}. The nonperturbative nature of this coupling allows one to maximize the speed, the single-shot fidelity, and the QND properties of the readout, while minimizing the effect of unwanted decay channels such as the Purcell effect [19].

B. Ancilla-cavity hybridization leading to polaritons

To use this coupling for reading out the state of the qubit, we strongly hybridize the ancilla and the cavity by setting their detuning $\Delta_{ac} = \omega_a - \omega_c$ to values comparable to or smaller than their transverse coupling $g_{ac}/2\pi = 295$ MHz. At this operation point, $|\Delta_{ac}| \lesssim g_{ac}$, this hybridization leads to two new normal modes called upper and lower polariton modes, $\hat{c}_u$ and $\hat{c}_l$, respectively for the higher and lower in frequency. They are a linear combination of ancilla and cavity fields [see Figs. 1(a) and 1(b)]. They are given by a rotation $\hat{c}_u = \cos(\theta)\hat{a} + \sin(\theta)\hat{c}$, and $\hat{c}_l = \cos(\theta)\hat{c} - \sin(\theta)\hat{a}$, where the cavity-ancilla hybridization angle reads $\tan(2\theta) = 2g_{ac}/\Delta_{ac}$. At resonance ($\Delta_{ac} = 0$,

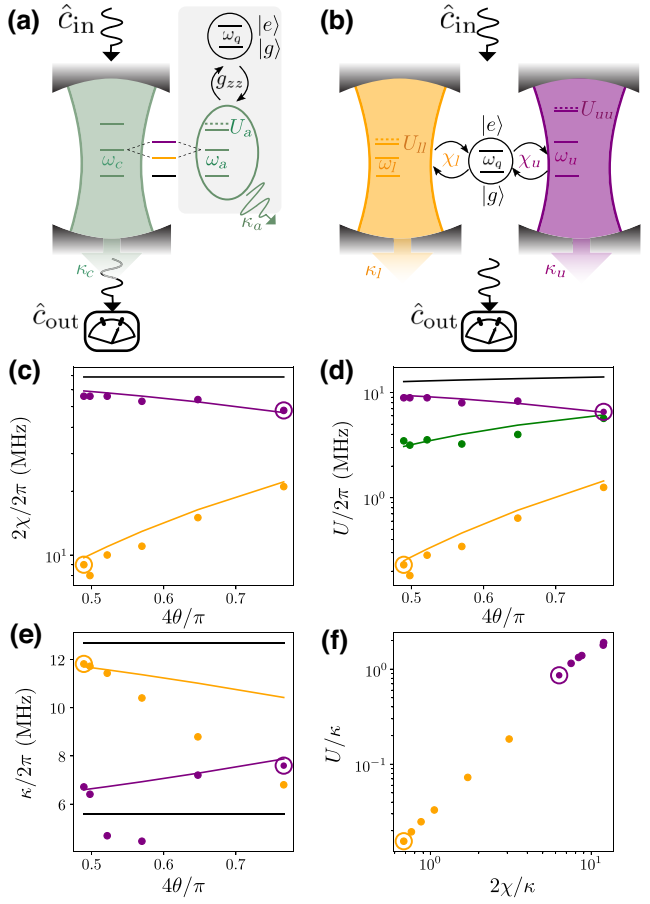

FIG. 1. (a) Scheme of the setup. The cavity mode $\hat{c}$ of frequency ω_c is strongly coupled to an anharmonic ancilla mode of frequency ω_a and self-Kerr nonlinearity U_a. The ancilla is also coupled to the qubit via a nonperturbative cross-Kerr-coupling of rate g_{zz}. To perform readout, we send a coherent signal on the input of the cavity mode $\hat{c}_{\text{in}}$ and measure the transmitted cavity output field $\hat{c}_{\text{out}}$. (b) Representation of the system in terms of cavity-ancilla polariton modes. Lower and upper polariton modes have distinct frequencies ω_l and ω_u, respectively, as well as different self-Kerr nonlinearities U_l and U_u inherited from the ancilla. Both polaritons are independently coupled to the qubit via cross-Kerr terms χ_l and χ_u, which allows us to use these polariton modes as direct meters of the qubit states. The readout can be extracted from the same output field c_{out} due to the polariton leakage rates κ_l and κ_u. (c)–(e) Measurements (dots) and predictions (lines) for lower polariton $j = l$ (orange) and upper polariton $j = u$ (purple) as functions of the hybridization angle θ of (c) the nonperturbative qubit-polariton cross-Kerr χ_j, (d) the self-Kerr U_{jj} and interpolariton cross-Kerr U_{ul} (green), and (e) the polariton decay rates κ_j. The predictions are calculated from the polariton model in Eqs. (2) and (3) using initial parameters g_{zz}, U_a, κ_c, and κ_a and plotted as black lines in panels (c)–(e), respectively. (f) Normalized self-Kerr polariton nonlinearity U_{jj}/κ_j versus normalized qubit-polariton cross-Kerr-coupling $2\chi_j/\kappa_j$ for lower and upper polaritons. In panels (c)–(f), the working points in the present work and in Ref. [19] are marked by a purple and orange circles, respectively.

$\theta = \pi/4$), the two modes are completely hybridized into equal symmetric and antisymmetric superpositions, while at large detuning ($|\Delta_{ac}| \gg g_{ac}$, $\theta \to 0$), the two normal modes tend to approach the bare ancilla and cavity modes.

In terms of these polariton modes and using the rotating-wave approximation, the total Hamiltonian takes the form

$$\frac{\hat{H}_p}{\hbar} = \frac{\omega_q}{2}\hat{\sigma}_z - \sum_{j=u,l}\chi_j \hat{c}_j^\dagger \hat{c}_j \hat{\sigma}_z + \sum_{j=u,l}\left(\omega_j \hat{c}_j^\dagger \hat{c}_j - \frac{U_{jj}}{2}\hat{c}_j^{\dagger 2}\hat{c}_j^2\right) - U_{ul}\hat{c}_l^\dagger \hat{c}_l \hat{c}_u^\dagger \hat{c}_u, \tag{2}$$

where $\omega_u = \sin^2(\theta)\omega_c + \cos^2(\theta)\omega_a + \sin(2\theta)g_{ac}$ and $\omega_l = \cos^2(\theta)\omega_c + \sin^2(\theta)\omega_a - \sin(2\theta)g_{ac}$ are the frequencies of the upper and lower polariton modes, respectively. Each polariton mode is in some proportion cavitylike and therefore can be probed in transmission and used for readout. Similarly, each polariton is also ancillalike and thus inherits nonlinearities from the ancilla, notably the *nonperturbative* cross-Kerr-coupling to the qubit. The corresponding interaction strengths read $\chi_u = g_{zz}\cos^2(\theta)$ and $\chi_l = g_{zz}\sin^2(\theta)$, for the upper and lower polariton, respectively.

Each polariton also inherits an anharmonicity from the ancilla given by $U_{ll} = \sin^4(\theta)U_a$ and $U_{uu} = \cos^4(\theta)U_a$. They also acquire a cross-anharmonicity or cross-Kerr interaction $U_{ul} = \sin^2(2\theta)U_a/2$, a coupling similar to the dispersive interaction that still occurs even beyond the dispersive regime [40]. Finally, the polaritons have effective decay rates given by a combination of the bare ancilla κ_a and cavity κ_c decay rates as (cf. Appendix C)

$$\begin{aligned}\kappa_u &= \kappa_c \sin^2(\theta) + \kappa_a \cos^2(\theta),\\ \kappa_l &= \kappa_c \cos^2(\theta) + \kappa_a \sin^2(\theta).\end{aligned} \tag{3}$$

C. Tuning hybridization

The ancilla can be tuned at discrete frequencies independently of the qubit and cavity. This is possible because the transmon molecule possesses two superconducting loops of different sizes with a high area ratio of 26 (see Appendixes A and B). Using one external coil, we can thus tune with a step precision of $\Phi_0/26$ the flux determining the ancilla frequency while the loop defining the qubit frequency still experiences an integer value of flux quantum Φ_0. This allows us to tune the hybridization conditions and thus the different parameters in Eqs. (2) and (3). We extracted these parameters [see Figs. 1(c)–1(f)] as functions of the hybridization angle by measuring at different flux points.

The nonperturbative cross-Kerr-couplings χ_l and χ_u are well fitted by a bare qubit-ancilla cross-Kerr-coupling $g_{zz}/2\pi = 34.5$ MHz [Fig. 1(c)]. The polariton's self-Kerr and cross-Kerr-couplings U_{ll}, U_{uu}, and U_{lu} are well fitted with the polariton model with a bare ancilla anharmonicity

$U_a/2\pi = 13.5$ MHz [Fig. 1(d)]. The polariton decay rates are only qualitatively fitted by the polariton model [Fig. 1(e)] with bare cavity and bare ancilla decay rates $\kappa_c/2\pi = 12.7$ MHz and $\kappa_a/2\pi = 5.6$ MHz. Discrepancies may be explained by the fact that the bare ancilla decay rate can vary with its frequency due to the presence of other losses like fluctuating two-level systems, or that there is residual parasitic transverse coupling between the ancilla and cavity with the qubit (see Ref. [19]).

Thanks to the hybridization tunability, we can set different regimes [Fig. 1(f)] for the polariton meters to read out the qubit. In Ref. [19], we focused on the linear response of the lower polariton, which presents a small self-Kerr $U/\kappa = 0.017$ at the moderate drive $\bar{n} \approx 2 \ll N_{\mathrm{crit}}$. This linear regime is obtained at the zero flux point ($\Phi/\Phi_0 = 0$) where the lower polariton is mostly cavitylike. In this work, we focus on a different regime where the anharmonicity is comparable to dissipation ($U \sim \kappa$). This is obtained for the upper polariton at $\Phi/\Phi_0 = 5$ when the ancilla is close to resonance with the cavity ($|\Delta_{ac}| \lesssim g_{ac}$). The hybridization is close to maximum, the upper polariton inherits from the ancilla an anharmonicity $U_{uu}/2\pi = 6.5$ MHz, and has a loss decay $\kappa_u/2\pi = 7.6$ MHz. At this working point, the cross-Kerr-coupling to the qubit is the dominant parameter, with $\chi_u/2\pi = 24$ MHz. All other parameters for these two flux points are summarized in Table I.

III. QUBIT-DEPENDENT POLARITONS RESPONSE

At time scales much shorter than the qubit's lifetime, $t \ll T_1$, the qubit state remains static in our setup and its main effect is to induce a qubit-dependent shift on the ancilla frequency as

$$\omega_a \to \bar{\omega}_a^{(\eta)} = \omega_a - g_{zz}\langle\hat{\sigma}_z\rangle_\eta, \tag{4}$$

where $\langle\hat{\sigma}_z\rangle_e = +1$ when the qubit is prepared in the excited state $\eta = e$ and $\langle\hat{\sigma}_z\rangle_g = -1$ when the qubit is in the ground state $\eta = g$. In terms of polaritons [Eq. (2)], this translates to a similar qubit-dependent shift on each polariton mode $j = u, l$ as

$$\omega_j \to \bar{\omega}_j^{(\eta)} = \omega_j - \chi_j\langle\hat{\sigma}_z\rangle_\eta, \tag{5}$$

as well as to a change in the hybridization angle as $\theta \to \arctan[2g_{ac}/(\bar{\omega}_a^{(\eta)} - \omega_c)]/2$.

To observe this qubit-dependent shift on the polaritons experimentally, we drive the cavity with a coherent field $\langle\hat{c}_{\mathrm{in}}\rangle = i(\Omega_c/\sqrt{\kappa_c})e^{-i\omega_d t}$ of frequency ω_d and amplitude Ω_c. We then perform homodyne detection at the transmission output of the cavity $\langle\hat{c}_{\mathrm{out}}\rangle_\eta = \sqrt{\kappa_c}\langle\hat{c}\rangle_\eta$, which contains information of the qubit state $\eta = g, e$ and of the polaritons as $\langle\hat{c}_{\mathrm{out}}\rangle_\eta = \sqrt{\kappa_c}(\sin(\theta)\langle\hat{c}_u\rangle_\eta + \cos(\theta)\langle\hat{c}_l\rangle_\eta)$. The experimental results are shown in Fig. 2(a), where we display the average pointer distance,

$$D_{eg} = |\langle\hat{c}_{\mathrm{out}}\rangle_e - \langle\hat{c}_{\mathrm{out}}\rangle_g|, \tag{6}$$

as a function of drive frequency ω_d and power P_{in}, which relates to the amplitude as $\Omega_c = \sqrt{\kappa_c P_{\mathrm{in}}/\hbar\omega_d}$. For this, we integrate over a 500-ns square readout pulse after preparing the qubit in its excited state ($\langle\hat{c}_{\mathrm{out}}\rangle_e$) or in its ground state ($\langle\hat{c}_{\mathrm{out}}\rangle_g$) by applying a 30-ns square π pulse or not. The input power y axis P_{in} is calibrated knowing the room-temperature power and the attenuation in the input line. The color bar of D_{eg} is calibrated knowing the gain of the output line. For both calibrations of the input and output line, we assumed the calibrations to be flat in frequency, which is true in our frequency window up to ± 1 dB.

As a first approximation, we consider both polaritons independent by neglecting their mutual coupling U_{ul}. It is thus possible to find a simple semiclassical model that properly describes our measurements up to moderate powers. When reaching a quasisteady state $1/\kappa_c \ll t \ll T_1$, the polariton amplitudes are solutions of the nonlinear equations (cf. Appendix C),

$$\langle\hat{c}_j\rangle_\eta = \frac{-i\Omega_j}{\kappa_j/2 - i(\omega_d - \bar{\omega}_j^{(\eta)} + U_{jj}|\langle\hat{c}_j\rangle_\eta|^2)}, \tag{7}$$

with effective polariton driving strengths $\Omega_u = \sin(\theta)\Omega_c$ and $\Omega_l = \cos(\theta)\Omega_c$. For very weak driving, we can further neglect the term U_{jj} in Eq. (7) and obtain the standard Lorentzian line shapes. In this linear regime ($P_{\mathrm{in}} \lesssim -112$ dBm), we observe four peaks in D_{eg} at the qubit-dependent polariton frequencies $\bar{\omega}_u^{(e)} = \omega_u + \chi_u = 2\pi \times 7.599$ GHz, $\bar{\omega}_l^{(e)} = \omega_l + \chi_l = 2\pi \times 6.963$ GHz, $\bar{\omega}_u^{(g)} = \omega_u - \chi_u = 2\pi \times 7.552$ GHz, and $\bar{\omega}_l^{(g)} = \omega_l - \chi_l = 2\pi \times 6.942$ GHz, which can be resolved due to the large cross-Kerr shifts $2\chi_j \gtrsim \kappa_j$.

The agreement between measurement and model (7) can be observed in Fig. 2(b), where we plot cross sections of D_{eg} for given input powers. As the driving power

TABLE I. Effective polariton parameters at two flux points, $\Phi/\Phi_0 = 0$ corresponding to the working point in Ref [19] and $\Phi/\Phi_0 = 5$ corresponding to the present working point.

Φ/Φ_0	$\omega_l/2\pi$	$\chi_l/2\pi$	$\kappa_l/2\pi$	$U_{ll}/2\pi$	$\bar{\theta}$
0	7.0335 GHz	4.5 MHz	11.8 MHz	0.2 MHz	0.384 rad
Φ/Φ_0	$\omega_u/2\pi$	$\chi_u/2\pi$	$\kappa_u/2\pi$	$U_{uu}/2\pi$	$\bar{\theta}$
5	7.575 GHz	24 MHz	7.6 MHz	6.5 MHz	0.602 rad

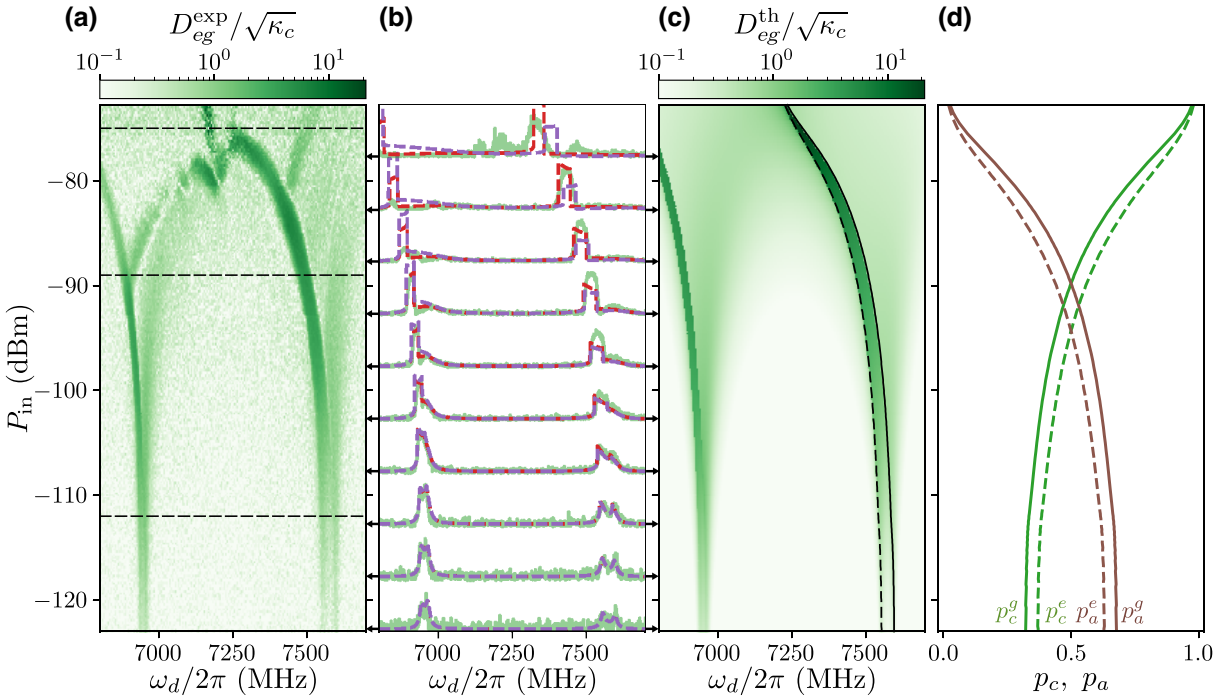

FIG. 2. (a) Measured mean distance D_{eg}^{exp} between the two pointer states of the qubit as a function of drive frequency ω_d and power P_{in}. Horizontal dashed lines are guides to the eyes, indicating different regimes of the system. From bottom to top: linear, nonlinear with self-Kerr, higher-order nonlinearities, and strongly driven bare cavity regime. (b) Cross sections of D_{eg} versus ω_d normalized by their experimental maximum value at fixed drive powers indicated by the arrows. In green, experimental data; in red, theoretical model in the ancilla-cavity basis [Eq. (8)]; and in dashed purple, theoretical model in the polariton basis [Eq. (7)]. (c) Computed D_{eg}^{th} using the model in Eq. (8). (d) Decomposition of upper polariton into cavity p_c^η (green) and ancilla p_a^η (brown) as a function of power P_{in} when the qubit is in $\eta = g$ (solid lines) or $\eta = e$ (dashed lines). The proportions p_c^η and p_a^η are computed using model (8) and following the drive frequency-power line $\omega_d(P_{\mathrm{in}})$ indicated by the solid and dashed lines in panel (c), corresponding to the qubit states $\eta = g$ and $\eta = e$, respectively.

increases, we need to consider the nonlinear term in the denominator of Eq. (7) and solve it self-consistently as a Duffing oscillator equation (cf. Appendix C). As a result, the polariton frequencies are downshifted due to their self-Kerr rate by an amount $\omega_j^{(\eta)} \to \bar{\omega}_j^{(\eta)} - U_{jj}|\langle\hat{c}_j\rangle_\eta|^2$, as shown in Figs. 2(a) and 2(b). Above a critical value of driving strength Ω_{crit}, the polaritons enter a bistability region, as can be hinted at by the sharp wavelike shape of the spectroscopic cross sections above $P_{\mathrm{in}} \gtrsim -108$ dBm in Fig. 2(b). Contrary to the case of only one nonlinear resonator, here Eq. (7) presents two bistability zones close to each polariton frequency, similarly to two coupled nonlinear resonators [37]. This bistability region for the upper polariton is studied in Sec. IV.

For the upper polariton, the effective model in Eq. (7) works well up to $P_{\mathrm{in}} \lesssim -89$ dBm as indicated by the middle horizontal line in Fig. 2(a), but needs to be refined at higher power. Indeed, describing a polariton by a fixed cavity-ancilla hybridization angle is no longer accurate at high power. As the driving power increases, the ancilla effectively modifies its frequency as $\bar{\omega}_a^{(\eta)} \to \bar{\omega}_a^{(\eta)} - U_a|\langle\hat{a}\rangle_\eta|^2$, which further modifies the hybridization condition as $\theta \to \arctan\left(2g_{ac}/(\omega_a^{(\eta)} - U_a|\langle\hat{a}\rangle_\eta|^2 - \omega_c)\right)/2$.

To achieve a more complete description of the circuit, we consider the dynamics in the cavity-ancilla basis. As shown in Appendix C, we can still neglect quantum fluctuations, obtaining the following nonlinear system of equations for the quasisteady-state amplitudes:

$$\begin{aligned}
&[\kappa_c/2 - i(\omega_d - \omega_c)]\langle\hat{c}\rangle_\eta + ig_{ac}\langle\hat{a}\rangle_\eta + i\Omega_c = 0,\\
&[\kappa_a/2 - i(\omega_d - \bar{\omega}_a^{(\eta)} + U_a|\langle\hat{a}\rangle_\eta|^2)]\langle\hat{a}\rangle_\eta + ig_{ac}\langle\hat{c}\rangle_\eta = 0.
\end{aligned} \tag{8}$$

We map these equations to a standard Duffing oscillator polynomial equation of order three (see Appendix C), which can have two stable solutions and one unstable solution (or vice versa) depending on the driving frequency $\omega_d/2\pi$ and amplitude Ω_c.

In Figs. 2(b) and 2(c) we show the theoretical prediction, which agrees well with the cavity transmission measurements up to large powers. The model in Eq. (7),

which considers two independent polaritons, agrees well with the model in Eq. (8), which includes the coupling between polaritons, in a wide range of input power, up to $\gtrsim -89$ dBm. We conclude that the polariton modes are nearly uncoupled and thus can be used as independent meters for the qubit readout. Nevertheless, for calculation purposes, we will still perform many calculations using the ancilla-cavity basis in Eq. (8) rather than Eq. (7).

From the numerical simulation of Eq. (8), we also extract more information about the decomposition of the polariton modes in terms of cavity and ancilla components. In particular, we compute for both qubit states η the cavity and ancilla population proportions, $p_c^\eta = |\langle\hat{c}\rangle_\eta|^2/(|\langle\hat{c}\rangle_\eta|^2 + |\langle\hat{a}\rangle_\eta|^2)$ and $p_a^\eta = |\langle\hat{a}\rangle_\eta|^2/(|\langle\hat{c}\rangle_\eta|^2 + |\langle\hat{a}\rangle_\eta|^2)$, along the upper polariton branch ω_d as a function of $P_{\rm in}$. The ancilla-cavity proportions depend on the qubit state as it shifts the ancilla frequency by $2g_{zz}$. At low power, the upper polariton is more ancillalike than cavitylike, while it is the opposite at large power. Effective ancilla-cavity resonance can be achieved for $|\langle a\rangle_\eta|^2 = (\bar{\omega}_a^{(\eta)} - \omega_c)/U_a$, where both polaritons become 50:50 ancillalike and cavitylike.

At even further input power, branches going to upward frequencies with input power start to appear in the measurement [Fig. 2(a)]. These features are not captured by our numerical model. We believe they are due to neglected higher nonlinear terms in the anharmonic ancilla mode, like the sixth order, which has an opposite sign to the fourth-order self-Kerr term. The dynamics become more and more complex and is beyond the scope of this paper. However, we find it worthwhile to note that, for a large enough driving power ($P_{\rm in} \geq -75$ dBm in our case), the system reaches a regime where the polariton physics disappears and the qubit state can be read out close to the bare cavity frequency $\omega_c/2\pi = 7.169$ GHz. This behavior appears to be similar to the quantum-to-classical transition physics as in Ref. [41] resulting in a destructive readout of the qubit state. At this high power, the ancilla is effectively far detuned from the cavity ($\theta \to 0$), and the upper polariton is becoming more and more cavitylike until only the bare cavity is recovered [Fig. 2(d)].

IV. QUBIT-DEPENDENT UPPER POLARITON BISTABILITY REGIONS

We now focus on frequencies around the upper polariton mode, and we study the bistability region in detail. As commented in the previous section, above a certain driving strength $\Omega_{\rm crit}$, the nonlinear polariton can have two stable quasisteady states. When crossing a bistability zone (where two stable solutions coexist), the system presents hysteretic behavior. For a fixed drive frequency, and a ramp up in amplitude $\dot{\Omega}_c(t) > 0$, the polariton bifurcates from a stable low-amplitude output to a stable high-amplitude output when crossing the point $B_\eta^{\rm up}(\omega_d, P_{\rm in})$ [see Fig. 3(a)]. Reciprocally, for a ramp down in amplitude $\dot{\Omega}_c(t) < 0$, the polariton bifurcates from a high-amplitude to a low-amplitude output when crossing a different point $B_\eta^{\rm down}(\omega_d, P_{\rm in}) < B_\eta^{\rm up}(\omega_d, P_{\rm in})$. To characterize the bistability zone for the upper polariton, we measure the distance,

$$D_\eta^{ud} = |\langle\hat{c}_{\rm out}\rangle_\eta^{\rm up} - \langle\hat{c}_{\rm out}\rangle_\eta^{\rm down}|, \tag{9}$$

which compares the output amplitude $\langle\hat{c}_{\rm out}\rangle_\eta^{\rm up}$ measured during a 500-ns ramp up with the amplitude $\langle\hat{c}_{\rm out}\rangle_\eta^{\rm down}$ obtained during a 500-ns ramp down. Both amplitudes are averaged over 2000 realizations. The bistability region is identified by a nonzero hysteretic signal difference $D_\eta^{ud} \neq 0$, since, outside this region, we have $D_\eta^{ud} = 0$. Remarkably, the bistability region of the upper polariton depends on the qubit state.

In Figs. 3(b) and 3(c) we display the measured D_η^{ud} and the bistability regions, for the qubit prepared in its ground state $\eta = g$ or excited state $\eta = e$, respectively. From the polariton's point of view, the qubit state shifts the upper polariton frequency by $2\chi_u$, and thus the bistability zone is also shifted by approximately $2\chi_u$. For both qubit states, the bistability zone and the hysteretic amplitude D_η^{ud} are well captured by Eq. (8).

V. QUBIT-STATE LATCHING READOUT

We measure the single-shot readout fidelity around the bistability zones, for the upper polariton, shown in Fig. 3. The results of the readout fidelity as a function of the frequency and power of the signal are shown in Fig. 4. We see that, for an amplitude below $B_e^{\rm up}$ (region I), the polariton does not bifurcate up for both qubit states. For an amplitude above $B_g^{\rm up}$ (region III), the polariton bifurcates up for both qubit states. Therefore, for regions I and III the readout fidelity is close to zero. This is not the case in region II, where we observe a very high fidelity. Here, at the beginning of the pulse, the input power is ramped up and crosses $B_e^{\rm up}$ but not $B_g^{\rm up}$. The upper polariton thus bifurcates up only if the qubit is in its excited state $|e\rangle$. During the pulse, the upper polariton will not bifurcate down as long as the input power does not fall below $B_g^{\rm down}$ or $B_e^{\rm down}$, even if the qubit has relaxed to its ground state $|g\rangle$. The high-amplitude output state is thus latched as long as input power is maintained above $B_\eta^{\rm down}$ even if the qubit has relaxed. The readout is thus less sensitive to qubit relaxation error. On the other hand, the readout is still sensitive to $|g\rangle \to |e\rangle$ transition error during measurement, for example, due to thermal excitations.

Using heralding to mitigate state preparation errors, we measure a maximum readout fidelity of $\mathcal{F}_{\rm RO} = 1 - [P(e|g) + P(g|e)]/2 = 98.6\%$ for a 500-ns square pulse. Here, $P(\alpha|\beta)$ is the error probability to read state α when the system was prepared in state β. This fidelity is obtained at 7.508 GHz drive frequency and -89 dBm

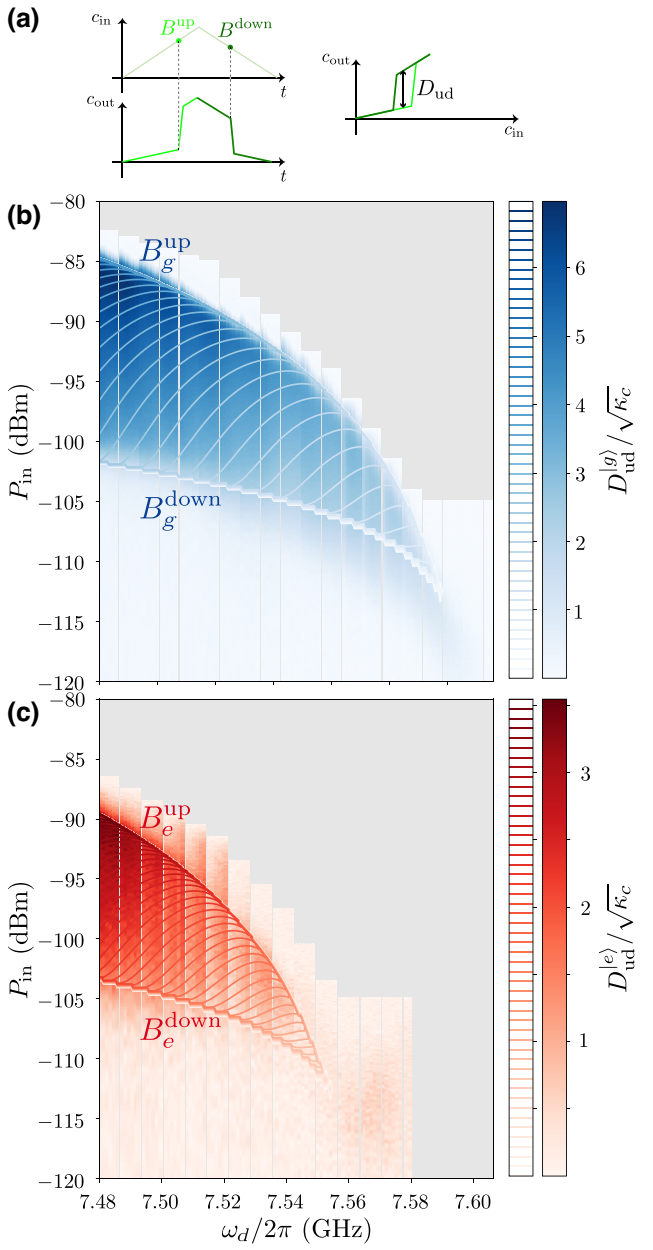

FIG. 3. Bistability region for the upper polariton mode. (a) Schematic of the hysteretic behavior. Left: Pulse sequence $\Omega_c(t)$ for a ramp up and ramp down applied to the cavity. This induces a bifurcation up (and down) in $\langle\hat{c}_{\text{out}}\rangle_\eta^{\text{up}}$ (and $\langle\hat{c}_{\text{out}}\rangle_\eta^{\text{down}}$), at different points B_η^{up} (and B_η^{down}). Right: Hysteretic signal D_η^{ud} is reconstructed from the output signal during the ramp up and ramp down. (b),(c) Measurement of the bistability hysteretic signal D_η^{ud} as a function of the input power P_{in} and frequency $\omega_d/2\pi$ when the qubit is prepared in (b) $\eta = g$ or in (c) $\eta = e$. The color map corresponds to the experimental data and the contour lines correspond to the theory in Eq. (8).

input power (see Fig. 4). At this working point, the photon number of the readout mode is around $\bar{n}_g \sim 0$ and $\bar{n}_e \sim 9$ when the qubit is $|g\rangle$ and $|e\rangle$, respectively. The error

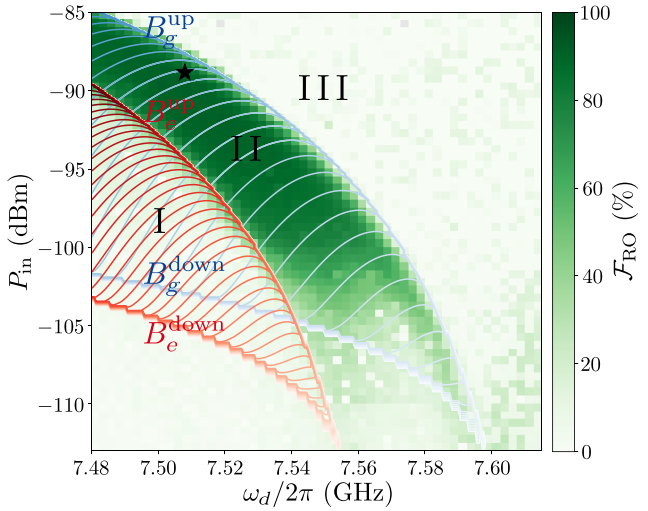

FIG. 4. Readout fidelity as a function of power and frequency. Superimposed are the computed bistability zones for the upper polariton as shown in Fig. 3. The point of maximum fidelity is indicated by a black star.

probabilities $P(\alpha|\beta)$ are obtained by counting the statistic with thresholding from the readout histograms over 10^5 repetitions where the qubit is prepared either in its ground or excited state. We extract $P(e|g) = 0.9 \pm 0.03\%$ and $P(g|e) = 1.9 \pm 0.05\%$ where the uncertainty comes from the finite number of repetitions. During the readout integration time $t_{\text{int}} = 500$ ns, we would expect the qubit to have relaxed around $1 - e^{-t_{\text{int}}/2T_1} \simeq 8\%$ of the times. However, thanks to the latching bifurcation mechanism, this error is strongly reduced to around $1 - e^{-t_b/2T_1}$, where t_b is the time to bifurcate up to the high-amplitude state, which is much smaller than the readout integration time t_{int}.

Assuming $t_b \simeq \kappa_u^{-1} = 21$ ns as a rough estimate, we thus calculate 0.3% error due to qubit relaxation before bifurcation within $P(g|e)$. We also estimate 0.1% error due to overlaps between the two Gaussians corresponding to each qubit state, 0.4% of heralding preparation error due to thermal excitations between the heralding and the readout pulse, and 1% of gate infidelity due to the finite duration of the π pulse and finite coherence time. Within $P(e|g)$, we estimate 0.1% error due to overlaps between the two Gaussians corresponding to each qubit state, 0.4% of heralding preparation error due to thermal excitations between the heralding and the readout pulse, and 0.2% error due to thermal excitation during the readout. The remaining readout infidelity of 0.15% (0.2% in $P(e|g)$ and 0.1% in $P(g|e)$) could be attributed to the wrong bifurcation event due to noise and uncertainty on the input power of the coherent drive. We believe this wrong bifurcation event error to be small thanks to the large shift $2\chi_u/2\pi = 48$ MHz allowing us to work with input power far enough from the B_η^{down} and B_η^{up} points. This error could be further suppressed in

the future by optimizing the driving power and frequency working point and the readout pulse shape.

The state of the qubit can thus be read out in a single-shot manner without any external quantum-limited amplifier. This is accomplished thanks to the qubit-state-dependent bistability and enhanced by a latching mechanism. Here, this regime is achieved at low photon number (about 9) and is differentiated strongly from the very high photon number like in Refs [41,42]. Contrary to the case of *in situ* JBA with transverse interaction to the qubit [22,43,44], here a large readout shift $\chi_u > \kappa_u, U_{uu}$ is possible without suffering from Purcell decay thanks to the nonperturbative nature of the cross-Kerr-coupling (see Appendix D for comparison). Using a two-step pulse [43] or shelving techniques [43,45,46], the errors due to wrong bifurcation events and relaxation before bifurcation may be reduced even further. With a readily achievable qubit T_1 and T_2 ten times greater than the current sample, the false qubit preparation and the transitions before bifurcation errors could be suppressed to 0.1%. Moreover, by adding an external quantum-limited amplifier, the overlap error can be erased, and the input readout power further reduced, thus limiting backaction on the qubit. Taking into account the whole, readout fidelity beyond 99.9% can be achieved.

VI. CONCLUSIONS AND OUTLOOK

Using a transmon molecule inside a cavity, we investigated transmon-qubit readout based on polariton meters. In particular, we studied the nonlinear response of polariton modes to a strong drive leading to a hysteretic bifurcation arising from the bistability of the upper polariton. Leveraging this effect, a latchinglike readout with 98.6% readout fidelity has been achieved without external quantum-limited amplification. This result is obtained in the mesoscopic regime when the polariton meter's amplitude is limited to a few photon number. Because of the nonperturbative cross-Kerr-coupling between the qubit and the readout polariton modes, the qubit does not suffer from Purcell decay.

A bifurcation amplifier of the qubit state with a large readout shift $2\chi > \kappa$ without deteriorating the qubit lifetime is thus possible and has been demonstrated. Such a readout with *in situ* amplification could reach quantum detection efficiency close to one by optimizing the techniques presented here. To this end, imperfections can be systematically studied and parameters recalibrated using recent QND detector tomography protocols [7,8,47]. Because of its flux tunability, our platform is also well suited for a systematic study of qubit readout performances as function of χ, κ, and U.

All the above properties make the transmon molecule inside a resonator a promising building block for implementing high-quality multiplexed readout in multiqubit devices. Indeed, multiple transmon molecules could be simultaneously measured by coupling dedicated resonators to a common transmission line, similarly as done in multiqubit transmon platforms [48]. Although our scheme may be *a priori* slightly more complicated than the usual qubit-resonator-Purcell filter building blocks, which also involve three modes, the possibility of nonperturbative cross-Kerr-couplings can strongly increase the speed and QND quality of the readout. This is particularly crucial for large-scale protocols with repetitive measurements [49–51]. In particular, our scheme allows qubits to induce large readout shifts $2\chi > \kappa$ while still having large detuning to readout modes, thereby mitigating frequency crowding, enhancing speed, and suppressing non-QND errors originating from residual Purcell-like effects [19] or measurement-induced state transitions within and beyond the rotating-wave approximation [12,52]. In addition, having an intrinsic and *in situ* amplification at each qubit can enable a large quantum detection efficiency, which can allow for a high signal-to-noise ratio even when strongly splitting the readout pulse to perform scalable multiqubit measurements.

Finally, the transmon molecule circuit is also promising for other readout schemes using polaritons as an *in situ* Josephson parametric dimer or JPA [37,38]. This can be achieved through degenerate pumping either below the critical bistability points of each polariton or in between the frequencies of the two polaritons. Implementing these strategies holds the potential to further enhance the quantum efficiency and performance of the readout process in future experiments.

ACKNOWLEDGMENTS

The authors thank D. Vion and E. Dumur for fruitful discussions. R.D. acknowledges funding from CFM pour la recherche. V.M., C.M., and O.B. acknowledge support from ANR REQUIEM (ANR-17-CE24-0012-01) and ANR OCTAVES (ANR-21-CE47-0007-01). Work in Madrid is funded by the Spanish project PGC2018-094792-B-I00 (MCIU/AEI/FEDER, UE), CSIC Interdisciplinary Thematic Platform (PTI+) on Quantum Technologies (PTI-QTEP+), and Proyecto Sinergico CAM 2020 Y2020/TCS-6545 (NanoQuCo-CM). T.R. further acknowledges support from the Juan de la Cierva fellowship IJC2019-040260-I, the Ramón y Cajal program RYC2021-032473-I, financed by MCIN/AEI/10.13039/50 1100011033 and the European Union NextGenerationEU/PRTR.

APPENDIX A: SAMPLE AND MICROWAVE WIRING

In this appendix, we describe the experimental setup. The device consists of an aluminum Josephson circuit realizing a transmon molecule and described by the lumped element circuit of Fig. 5(d). The circuit is deposited on an intrinsic silicon wafer as shown in Fig. 5(c) and inserted

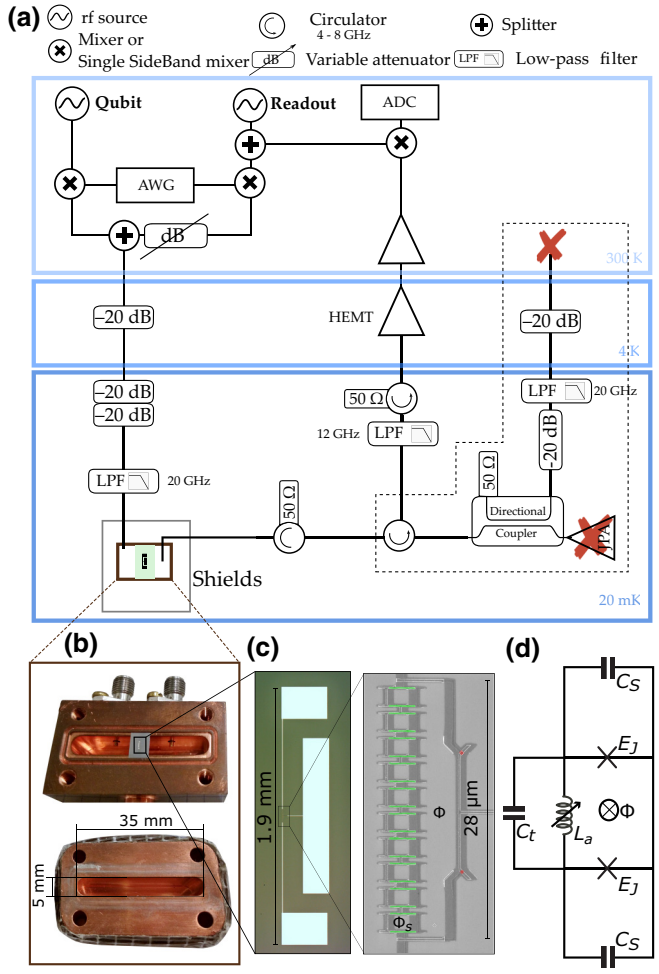

FIG. 5. (a) Schematic of the experimental setup. Even though a JPA is present, it is not pumped in the current work and so does not bring amplification. As our reported readout does not require an external quantum-limited amplifier, the part framed with the dashed line can be removed in order to further optimize the output line and enhance the readout performance. (b) Picture of the two parts of the 3D oxygen-free high-conductivity (OFHC) copper cavity with the input-output pin connectors. The sample is placed at the center of the cavity. (c) Optical microscope and SEM pictures of the transmon molecule sample. The Josephson junctions are highlighted in red. The superconducting quantum interference device (SQUID) Josephson junctions implementing the coupling inductance L_a are highlighted in green. (d) Lumped element circuit of the transmon molecule.

in a 3D copper cavity [Fig. 5(b)]. The transmon molecule Hamiltonian is described in the following appendix.

To measure the transmon molecule, we insert the silicon chip inside a 3D copper cavity with a volume of $24.5 \times 5 \times 35$ mm^3 [cf. Fig. 5(b)]. The cavity mode considered is the fundamental TE_{101} mode.

The schematic of the experimental setup is shown in Fig. 5(a). Qubit and readout pulses are sent through the same input line. The output line carries the readout signal to a high-electron-mobility transistor (HEMT) through two circulators to prevent any noisy microwave signal going back to the cavity. The output line was wired to include a JPA, which was turned off for the present study. Consequently, the transmitted signal passes through two circulators and a directional coupler before being reflected on the JPA. As the JPA was not pumped, no amplifications were performed. Then the reflected signal passes again through the directional coupler and circulator before entering the first amplification stage with the HEMT amplifier. This not-optimal output line wiring does not prevent us achieving high-fidelity readout. However, the readout performances could be further improved by removing the JPA-related wiring that involves insertion and propagation losses. At room temperature, the signal is down-converted to dc voltages via an in-phase and quadrature (IQ) mixer and digitized at 1 GS/s using an analog-to-digital converter (ADC). Finally, the signal is digitally integrated.

APPENDIX B: TRANSMON MOLECULE HAMILTONIAN

In this appendix, we derive the circuit Hamiltonian of the transmon molecule. The molecule is realized by two identical transmon qubits with Josephson energy E_J and capacitance C_S, coupled through a parallel LC circuit with inductance L_a and capacitance C_t [see Fig. 5(d)]. Here, C_S represents the capacitance between either small rectangular electrode and the longer central one, while C_t represents the capacitance between the two small rectangular electrodes. The coupling inductor L_a is implemented by a chain of 10 small SQUID loops of area S_{SQUID}, which are tunable by an external flux Φ_S [cf. Fig. 5(c)]. The circuit also contains a large loop of enclosed area A that is approximately $r = A/S_{\mathrm{SQUID}} \simeq 26$ times larger than the SQUIDs. Consequently, the flux $\Phi = r\Phi_S$ generates a circulating current passing through both L_a and the two small Josephson junctions of the transmons.

As already discussed in previous work [19], when the applied flux satisfies $\Phi = n\Phi_0$ (with n an integer and Φ_0 the magnetic flux quantum), the dynamics of the system effectively behaves as a single-transmon qubit with cross-Kerr-coupling to a slightly anharmonic ancilla mode, described by the Hamiltonian

$$\hat{H}_{\mathrm{mol}} = 4E_{C_q}\hat{n}_q^2 - 2E_J\cos(\hat{\varphi}_q) + 4E_{C_a}\hat{n}_a^2 - 2E_J\left(\cos(\hat{\varphi}_a) - \frac{L_J}{L_a(n)}\hat{\varphi}_a^2\right) - \frac{E_J}{2}\hat{\varphi}_q^2\hat{\varphi}_a^2 + \mathcal{O}^6. \tag{B1}$$

Here, the phase average $\hat{\varphi}_q$ and phase difference $\hat{\varphi}_a$ between the two Josephson junctions describe the effective transmon qubit and the ancilla mode, respectively. Their conjugate charge number operators are denoted by

$\hat{n}_q$ and $\hat{n}_a$. The charging energies of qubit and ancilla are given by $E_{C_q} = e^2/(2C_q)$ and $E_{C_a} = e^2/(2C_a)$, with effective capacitances $C_q = 2C_S$ and $C_a = 2(C_S + 2C_t)$, respectively.

We considered the system in the transmon regime, $E_J \gg E_{C_q}, E_{C_a}$, so that $\hat{\varphi}_q, \hat{\varphi}_a \ll 1$ and therefore expanded the coupling term between $\hat{\varphi}_q$ and $\hat{\varphi}_a$ up to fourth order in the phases. In addition, $L_J = (\Phi_0/2\pi)^2(1/E_J)$ describes the Josephson inductance of each junction and $L_a(n)$ denotes the value of the coupling inductance for given magnetic flux $\Phi_S = (n/r)\Phi_0$. Importantly, the last term in Eq. (B1) originates the nonlinear cross-Kerr-coupling between transmon qubit and ancilla as shown in the next subsection.

To express the Hamiltonian in the number representation, we exploit the analogy between the quadratic terms and the Hamiltonian of independent quantum harmonic oscillators with positions $\hat{x}_j = \hat{\varphi}_j$, momenta $\hat{p}_j = \hbar\hat{n}_j$, masses $m_j = \hbar^2/(8E_{C_j})$, and frequencies $\tilde{\omega}_j = \sqrt{8E_{J_j}E_{C_j}}/\hbar$, for qubit and ancilla ($j = q, a$), where we have defined the effective Josephson energies of qubit and ancilla as $E_{J_q} = 2E_J$ and $E_{J_a}(n) = 2E_J(1 + 2L_J/L_a(n))$, respectively. With these identifications, we can use the known results from the quantization of the quantum harmonic oscillator and express the phase and number operators as

$$\hat{\varphi}_q = \left(\frac{8E_{C_q}}{E_{J_q}}\right)^{1/4} \frac{(\hat{q} + \hat{q}^\dagger)}{\sqrt{2}}, \tag{B2}$$

$$\hat{n}_q = -i\left(\frac{E_{J_q}}{8E_{C_q}}\right)^{1/4} \frac{(\hat{q} - \hat{q}^\dagger)}{\sqrt{2}}, \tag{B3}$$

$$\hat{\varphi}_a = \left(\frac{8E_{C_a}}{E_{J_a}(n)}\right)^{1/4} \frac{(\hat{a} + \hat{a}^\dagger)}{\sqrt{2}}, \tag{B4}$$

$$\hat{n}_a = -i\left(\frac{E_{J_a}(n)}{8E_{C_a}}\right)^{1/4} \frac{(\hat{a} - \hat{a}^\dagger)}{\sqrt{2}}, \tag{B5}$$

where $\hat{q}$, $\hat{q}^\dagger$ and $\hat{a}$, $\hat{a}^\dagger$ are standard ladder operators for the qubit and ancilla modes, respectively.

Replacing expressions (B2)–(B5) into Eq. (B1), we diagonalize the quadratic terms of the circuit Hamiltonian, allowing us to interpret the qubit and ancilla modes as two coupled anharmonic oscillators described by

$$\frac{\hat{H}_{\text{mol}}}{\hbar} = \tilde{\omega}_q\hat{q}^\dagger\hat{q} + \frac{\alpha_q}{12}(\hat{q} + \hat{q}^\dagger)^4 + \tilde{\omega}_a\hat{a}^\dagger\hat{a} - \frac{U_a}{12}(\hat{a} + \hat{a}^\dagger)^4 - \frac{g_{zz}}{2}(\hat{q} + \hat{q}^\dagger)^2(\hat{a} + \hat{a}^\dagger)^2. \tag{B6}$$

Here, the anharmonicities of the qubit and ancilla are given by $\alpha_q = -E_{C_q}/\hbar$ and $U_a = (E_{C_a}/\hbar)(1 + 2L_J/L_a(n))^{-1}$, respectively, and $g_{zz} = \sqrt{\alpha_q U_a}$ is the strength of their cross-Kerr-coupling.

Considering a large enough anharmonicity $|\alpha_q|$, we can approximate the transmon qubit by its two lowest states, so that it can be fully described by Pauli operators, $\hat{\sigma}_z = 2\hat{q}^\dagger\hat{q} - 1$ and $\hat{\sigma}_- = \hat{q}$. Finally, adding the cavity mode $\hat{c}$, its coupling to the ancilla, and applying the rotating-wave approximation (RWA) to Eq. (B6), we recover Eq. (1) of the main text.

APPENDIX C: OPEN QUANTUM SYSTEM DESCRIPTION AND NONLINEAR STEADY-STATE DYNAMICS

In this appendix, we present details of the theoretical models to describe our setup as a nonlinear open quantum system. We also indicate the approximations and the specific nonlinear Duffing equations that we use to interpret the measured data.

1. Cavity-ancilla basis

For a timescale much shorter than the lifetime of the qubit, $t \ll T_1$, we can neglect the dynamics of the qubit, and therefore its only effect is to provide a static shift on the ancilla frequency depending on the qubit state. This is described by the system Hamiltonian $\hat{H}$ in Eq. (1). If we additionally take into account the dynamics induced by a coherent drive of strength Ω_c on the cavity, $\hat{H}_d = \hbar\Omega_c(\hat{c}e^{i\omega_d t} + \hat{c}^\dagger e^{-i\omega_d t})$, the total Hamiltonian $\hat{H}_{\text{tot}} = \hat{H} + \hat{H}_d$ in the rotating frame with respect to the drive frequency ω_d reads

$$\frac{\hat{H}_{\text{tot}}}{\hbar} = -(\omega_d - \bar{\omega}_a^{(\eta)})\hat{a}^\dagger\hat{a} - \frac{U_a}{2}\hat{a}^\dagger\hat{a}^\dagger\hat{a}\hat{a} - (\omega_d - \omega_c)\hat{c}^\dagger\hat{c} + g_{ac}(\hat{a}^\dagger\hat{c} + \hat{c}^\dagger\hat{a}) + \Omega_c(\hat{c} + \hat{c}^\dagger), \tag{C1}$$

where $\bar{\omega}_a^{(\eta)} = \omega_a - g_{zz}\langle\sigma_z\rangle_\eta$ is the qubit-dependent ancilla frequency. Considering the decay of the cavity κ_c and ancilla κ_a, the master equation for the density operator of the system $\hat{\rho}(t)$ reads

$$\dot{\hat{\rho}} = -i\left[\frac{\hat{H}_{\text{tot}}}{\hbar}, \hat{\rho}\right] + \kappa_c\mathcal{D}[\hat{c}]\hat{\rho} + \kappa_a\mathcal{D}[\hat{a}]\hat{\rho}. \tag{C2}$$

We consider a displacement transformation for the cavity and ancilla modes, $\hat{a} = \alpha(t) + \delta\hat{a}$ and $\hat{c} = \gamma(t) + \delta\hat{c}$, where $\delta\hat{a}$ and $\delta\hat{c}$ are quantum fluctuation operations around the classical mean displacements $\alpha(t)$ and $\gamma(t)$, respectively. The dynamics of the classical fields are given by the coupled nonlinear equations

$$\begin{aligned}\dot{\alpha} &= -[\kappa_a/2 - i(\omega_d - \bar{\omega}_a^{(\eta)})]\alpha - ig_{ac}\gamma + iU_a|\alpha|^2\alpha,\\ \dot{\gamma} &= -[\kappa_c/2 - i(\omega_d - \omega_c)]\gamma - i\Omega_c - ig_{ac}\alpha,\end{aligned} \tag{C3}$$

whereas the dynamics of the quantum fluctuations is described by the master equation for the new density operator $\hat{\rho}_F(t)$,

$$\dot{\hat{\rho}}_F = -i\left[\frac{\hat{H}_F}{\hbar}, \hat{\rho}_F\right] + \kappa_c \mathcal{D}[\delta\hat{c}]\hat{\rho}_F + \kappa_a \mathcal{D}[\delta\hat{a}]\hat{\rho}_F. \quad \text{(C4)}$$

Here, the fluctuation Hamiltonian reads,

$$\begin{aligned}\frac{\hat{H}_F}{\hbar} = &-(\omega_d - \bar{\omega}_a^{(\eta)} + 2U_a|\alpha|^2)\delta\hat{a}^\dagger\delta\hat{a} + g_{ac}(\delta\hat{a}^\dagger\delta\hat{c} \\ &+ \delta\hat{c}^\dagger\delta\hat{a}) - (\omega_d - \omega_c)\delta\hat{c}^\dagger\delta\hat{c} \\ &- \frac{U_a}{2}[\alpha^2(\delta\hat{a}^\dagger)^2 + (\alpha^*)^2(\delta\hat{a})^2] - U_a[\alpha(\delta\hat{a}^\dagger)^2\delta\hat{a} \\ &+ \alpha^*\delta\hat{a}^\dagger\delta\hat{a}^2] - \frac{U_a}{2}(\delta\hat{a}^\dagger)^2(\delta\hat{a})^2. \quad \text{(C5)}\end{aligned}$$

Note that the dynamics in Eqs. (C3)–(C5) is equivalent to the original one in Eqs. (C1) and (C2), but the former equations are more convenient when quantum fluctuations are small, which is the case when driving the system with a strong coherent drive on the cavity Ω_c.

The steady-state solution for the classical displacements in Eqs. (C3) is obtained by first solving the following nonlinear algebraic Duffing oscillator for the ancilla,

$$[A - i(B + C|\alpha_{ss}|^2)]\alpha_{ss} = D, \quad \text{(C6)}$$

and then obtaining the solution for the cavity displacement as

$$\gamma_{ss} = \frac{-i(\Omega_c + g_{ac}\alpha_{ss})}{\kappa_c/2 - i(\omega_d - \omega_c)}. \quad \text{(C7)}$$

Note that in Eq. (C6) the parameters read $A = \kappa_a/2 + g_{ac}\,\mathrm{Re}(z)$, $B = \omega_d - \bar{\omega}_a^{(\eta)} - g_{ac}\,\mathrm{Im}(z)$, $C = U_a$, $D = -z\Omega_c$, and $z = g_{ac}/[\kappa_c/2 - i(\omega_d - \omega_c)]$. This Eq. (C6) is more conveniently solved in terms of a third-order polynomial,

$$C^2x^3 + 2BCx^2 + (A^2 + B^2)x - D = 0, \quad \text{(C8)}$$

for $x = |\alpha_{ss}|^2$. In this work, we numerically solve for Eq. (C8) and then determine the full ancilla displacements via $\alpha_{ss} = D/[A - i(B + Cx)]$ and Eq. (C7).

We checked numerically that in steady state $t \gg 1/\kappa_c$, the quantum fluctuations are always small with respect to the classical displacement, $|\langle\delta\hat{a}\rangle| \ll |\alpha_{ss}|$ and $|\langle\delta\hat{c}\rangle| \ll |\gamma_{ss}|$, and therefore it is a good approximation to completely neglect them, namely $\langle\hat{a}\rangle_\eta \approx \alpha_{ss}$ and $\langle\hat{c}\rangle_\eta \approx \gamma_{ss}$, as given by the solution of Eqs. (C6)–(C8). Under these approximations, Eq. (8) of the main text is valid.

In Sec. IV, when discussing the bistability of the upper polariton, we calculate the stable solutions after a ramp up and ramp down of the system by the solutions of Eq. (C8) with lowest and largest amplitude, respectively. This matches very well the measured data as indicated in Figs. 3(b) and 3(c).

2. Polariton basis

Starting from Eqs. (C1) and (C2) and doing a polariton transformation $\hat{c}_u = \cos(\theta)\hat{a} + \sin(\theta)\hat{c}$ and $\hat{c}_l = \cos(\theta)\hat{c} - \sin(\theta)\hat{a}$, as indicated in Sec. II B, we can describe the system by the master equation

$$\dot{\hat{\rho}}' = -i\left[\frac{\hat{H}^p_{\mathrm{tot}}}{\hbar}, \hat{\rho}'\right] + \sum_j \kappa_j \mathcal{D}[\delta\hat{c}_j]\hat{\rho}', \quad \text{(C9)}$$

where the total Hamiltonian for the polariton modes $\hat{c}_j$, considering the coherent drive in the rotating frame with frequency ω_d, reads

$$\begin{aligned}\frac{\hat{H}^p_{\mathrm{tot}}}{\hbar} = &\frac{\omega_q}{2}\hat{\sigma}_z - \sum_{j=u,l}\chi_j\hat{c}_j^\dagger\hat{c}_j\hat{\sigma}_z + \sum_{j=u,l}\left(\omega_j\hat{c}_j^\dagger\hat{c}_j - \frac{U_{jj}}{2}\hat{c}_j^{\dagger 2}\hat{c}_j^2\right) \\ &+ \sum_{j=u,l}\Omega_j(\hat{c}_j + \hat{c}_j^\dagger) - U_{ul}\hat{c}_l^\dagger\hat{c}_l\hat{c}_u^\dagger\hat{c}_u. \quad \text{(C10)}\end{aligned}$$

Here, the effective polariton driving strengths are given as in the main text as $\Omega_u = \sin(\theta)\Omega_c$ and $\Omega_l = \cos(\theta)\Omega_c$.

We can also apply a displacement transformation on the polariton operators, $\hat{c}_j = \gamma_j(t) + \delta\hat{c}_j$ and obtain an equivalent description, similar as done above for the cavity-ancilla basis. The classical displacements $\gamma_j(t)$ are described by the coupled nonlinear equations,

$$\begin{aligned}\dot{\gamma}_j = &-[\kappa_j/2 - i(\omega_d - \omega_j^{(\eta)})]\gamma_j - i\Omega_j \\ &+ iU_{jj}|\gamma_j|^2\gamma_j + iU_{ul}|\gamma_{-j}|^2\gamma_j. \quad \text{(C11)}\end{aligned}$$

The quantum fluctuations are described by a master equation,

$$\dot{\hat{\rho}}'_F = -i[\hat{H}^F_p, \hat{\rho}'_F] + \kappa_j \mathcal{D}[\delta\hat{c}_j]\hat{\rho}'_F. \quad \text{(C12)}$$

The Hamiltonian for the polariton quantum fluctuations $\hat{H}^F_p$ can be more compactly written using the identifications $\delta\hat{c}_u \to \delta\hat{c}_+$ and $\delta\hat{c}_l \to \delta\hat{c}_-$ as

$$\hat{H}_p^F = \sum_{j=\pm}\Bigg[-\left(\omega_d - \bar{\omega}_j^{(\eta)} + 2U_{jj}|\gamma_j|^2 + \frac{U_{ul}}{2}|\gamma_{-j}|^2\right)\delta\hat{c}_j^\dagger\delta\hat{c}_j - U_{jj}\gamma_j^*\delta\hat{c}_j^\dagger(\delta\hat{c}_j)^2 - U_{jj}\gamma_j(\delta\hat{c}_j^\dagger)^2\delta\hat{c}_j$$
$$-\frac{U_{jj}}{2}(\gamma_j)^2(\delta\hat{c}_j^\dagger)^2 - \frac{U_{jj}}{2}(\gamma_j^*)^2(\delta\hat{c}_j)^2 - \frac{U_{jj}}{2}(\delta\hat{c}_j^\dagger)^2(\delta\hat{c}_j)^2\Bigg] - U_{ul}\sum_{j=\pm}\Big[\gamma_j(\gamma_{-j}^*)\delta\hat{c}_j^\dagger\delta\hat{c}_{-j} + \gamma_{-j}^*\delta\hat{c}_j^\dagger\delta\hat{c}_j\delta\hat{c}_{-j}$$
$$+\gamma_{-j}\delta\hat{c}_{-j}^\dagger\delta\hat{c}_j^\dagger\delta\hat{c}_j + \frac{\gamma_j}{2}\gamma_{-j}\delta\hat{c}_j^\dagger\delta\hat{c}_{-j}^\dagger + \frac{1}{2}\gamma_j^*\gamma_{-j}^*\delta\hat{c}_j\delta\hat{c}_{-j} + \frac{1}{2}\delta\hat{c}_j^\dagger\delta\hat{c}_{-j}^\dagger\delta\hat{c}_j\delta\hat{c}_{-j}\Big]. \quad \text{(C13)}$$

Similarly, as for the cavity-ancilla basis, we checked numerically that quantum fluctuations are always small in our problem, $|\langle\delta\hat{c}_j\rangle| \ll |\gamma_j|$, and therefore we neglect them for simplicity $\langle\hat{c}_j\rangle_\eta \approx \gamma_j$.

In addition, we found that neglecting the coupling between polaritons U_{ul} is a good approximation to our data up to moderately large driving amplitudes Ω_c. This further simplifies the analysis of the nonlinear polariton meters of our setup, as they can be well modeled as independent modes. The quasisteady-state amplitudes of each polariton $\langle\hat{c}_j\rangle_\eta$ are solutions of standard Duffing oscillator equations of the form

$$[\kappa_j/2 - i(\omega_d - \bar{\omega}_j^{(\eta)} + U_{jj}|\langle\hat{c}_j\rangle_\eta|^2)]\langle\hat{c}_j\rangle_\eta = -i\Omega_j. \quad \text{(C14)}$$

This is Eq. (7) of the main text, which can be put in the same form as Eq. (C8) with $x_j = |\langle\hat{c}_j\rangle_\eta|^2$, $A_j = \kappa_j/2$, $B_j = \omega_d - \bar{\omega}_j^{(\eta)}$, $C_j = U_{jj}$, and $D_j = -i\Omega_j$. In this way we solve self-consistently for the occupation of each polariton mode $x_j = |\langle\hat{c}_j\rangle_\eta|^2$ first, and then we obtain the full solution for each mode independently as $\langle\hat{c}_j\rangle_\eta = D_j/[A_j - i(B_j + C_j x_j)]$.

APPENDIX D: COMPARISON WITH OTHER BIFURCATION READOUT

In Table II are summarized the χ, κ, U, N_{crit}, $\mathcal{F}_{\text{RO}}$, t_{int}, and T_1 values for our present work and for different references using a Josephson bifurcation amplifier or a Josephson parametric oscillator with dispersive interaction with a qubit. While κ is in the same order of magnitude, our cavity pull χ is much larger than in other references thanks to the nonperturbative nature of the cross-Kerr-coupling. Moreover, JBA is usually used in the case $U \ll \kappa$, meaning a large number of photons are required to attain the bistability zone, while in our case, $U \lesssim \kappa$, a photon number close to unity is sufficient to attain the bistability zone.

TABLE II. Readout system parameters for different references using a Josephson bifurcation amplifier or a Josephson parametric oscillator.

	Present work	Ref. [22]	Ref. [43]	Ref. [44]
$\chi/2\pi$ (MHz)	24	2.1	1.7	3.6
$\kappa/2\pi$ (MHz)	7.6	9.4	3.1	1.3
$U/2\pi$ (MHz)	6.5	(0.02)	0.3	0.03
N_{crit}	0.2	90.5	2.0	8.3
$\mathcal{F}_{\text{RO}}$ (%)	98.6	92	98.3	90.8
t_{int} (ns)	500	965	2025	600
T_1 (μs)	3.3	0.5	2.5	4.1

[1] T. Walter, P. Kurpiers, S. Gasparinetti, P. Magnard, A. Potočnik, Y. Salathé, M. Pechal, M. Mondal, M. Oppliger, C. Eichler, and A. Wallraff, Rapid high-fidelity single-shot dispersive readout of superconducting qubits, Phys. Rev. Appl. **7**, 054020 (2017).

[2] Y. Sunada, S. Kono, J. Ilves, S. Tamate, T. Sugiyama, Y. Tabuchi, and Y. Nakamura, Fast readout and reset of a superconducting qubit coupled to a resonator with an intrinsic Purcell filter, Phys. Rev. Appl. **17**, 044016 (2022).

[3] A. Blais, R.-S. Huang, A. Wallraff, S. M. Girvin, and R. J. Schoelkopf, Cavity quantum electrodynamics for superconducting electrical circuits: An architecture for quantum computation, Phys. Rev. A **69**, 062320 (2004).

[4] J. Koch, T. M. Yu, J. Gambetta, A. A. Houck, D. I. Schuster, J. Majer, A. Blais, M. H. Devoret, S. M. Girvin, and R. J. Schoelkopf, Charge-insensitive qubit design derived from the Cooper pair box, Phys. Rev. A **76**, 042319 (2007).

[5] J. Aumentado, Superconducting parametric amplifiers: The state of the art in Josephson parametric amplifiers, IEEE Microw. Mag. **21**, 45 (2020).

[6] A. A. Houck, J. A. Schreier, B. R. Johnson, J. M. Chow, J. Koch, J. M. Gambetta, D. I. Schuster, L. Frunzio, M. H. Devoret, S. M. Girvin, and R. J. Schoelkopf, Controlling the Spontaneous Emission of a Superconducting Transmon Qubit, Phys. Rev. Lett. **101**, 080502 (2008).

[7] L. Pereira, J. J. García-Ripoll, and T. Ramos, Complete Physical Characterization of Quantum Nondemolition Measurements via Tomography, Phys. Rev. Lett. **129**, 010402 (2022).

[8] L. Pereira, J. J. García-Ripoll, and T. Ramos, Parallel tomography of quantum non-demolition measurements in multi-qubit devices, npj Quantum Inf. **9**, 1 (2023).

[9] B. R. Johnson, M. D. Reed, A. A. Houck, D. I. Schuster, L. S. Bishop, E. Ginossar, J. M. Gambetta, L. DiCarlo, L. Frunzio, S. M. Girvin, and R. J. Schoelkopf, Quantum non-demolition detection of single microwave photons in a circuit, Nat. Phys. **6**, 663 (2010).

[10] Z. K. Minev, S. O. Mundhada, S. Shankar, P. Reinhold, R. Gutiérrez-Jáuregui, R. J. Schoelkopf, M. Mirrahimi, H. J. Carmichael, and M. H. Devoret, To catch and reverse a quantum jump mid-flight, Nature **570**, 200 (2019).

[11] R. Lescanne, L. Verney, Q. Ficheux, M. H. Devoret, B. Huard, M. Mirrahimi, and Z. Leghtas, Escape of a driven quantum Josephson circuit into unconfined states, Phys. Rev. Appl. **11**, 014030 (2019).

[12] M. Khezri, *et al.*, Measurement-induced state transitions in a superconducting qubit: Within the rotating wave approximation, ArXiv:2212.05097 (2022).

[13] R. Shillito, A. Petrescu, J. Cohen, J. Beall, M. Hauru, M. Ganahl, A. G. Lewis, G. Vidal, and A. Blais, Dynamics of transmon ionization, Phys. Rev. Appl. **18**, 034031 (2022).

[14] I. Diniz, E. Dumur, O. Buisson, and A. Auffèves, Ultrafast quantum nondemolition measurements based on a diamond-shaped artificial atom, Phys. Rev. A **87**, 033837 (2013).

[15] X. Wang, A. Miranowicz, and F. Nori, Ideal quantum nondemolition readout of a flux qubit without Purcell limitations, Phys. Rev. Appl. **12**, 064037 (2019).

[16] É. Dumur, B. Küng, A. K. Feofanov, T. Weissl, N. Roch, C. Naud, W. Guichard and O. Buisson, V-shaped superconducting artificial atom based on two inductively coupled transmons, Phys. Rev. B **92**, 020515(R) (2015).

[17] T. Roy, S. Kundu, M. Chand, S. Hazra, N. Nehra, R. Cosmic, A. Ranadive, M. P. Patankar, K. Damle, and R. Vijay, Implementation of pairwise longitudinal coupling in a three-qubit superconducting circuit, Phys. Rev. Appl. **7**, 054025 (2017).

[18] T. Roy, M. Chand, A. Bhattacharjee, S. Hazra, S. Kundu, K. Damle, and R. Vijay, Multimode superconducting circuits for realizing strongly coupled multiqubit processor units, Phys. Rev. A **98**, 052318 (2018).

[19] R. Dassonneville, T. Ramos, V. Milchakov, L. Planat, E. Dumur, F. Foroughi, J. Puertas, S. Leger, K. Bharadwaj, J. Delaforce, C. Naud, W. Hasch-Guichard, J. J. García-Ripoll, N. Roch, and O. Buisson, Fast High-Fidelity Quantum Nondemolition Qubit Readout via a Nonperturbative Cross-Kerr Coupling, Phys. Rev. X **10**, 011045 (2020).

[20] A. Lupaşcu, E. F. C. Driessen, L. Roschier, C. J. P. M. Harmans, and J. E. Mooij, High-Contrast Dispersive Readout of a Superconducting Flux Qubit Using a Nonlinear Resonator, Phys. Rev. Lett. **96**, 127003 (2006).

[21] R. Vijay, M. H. Devoret, and I. Siddiqi, Invited review article: The Josephson bifurcation amplifier, Rev. Sci. Instrum. **80**, 111101 (2009).

[22] F. Mallet, F. R. Ong, A. Palacios-Laloy, F. Nguyen, P. Bertet, D. Vion, and D. Esteve, Single-shot qubit readout in circuit quantum electrodynamics, Nat. Phys. **5**, 791 (2009).

[23] I. Siddiqi, R. Vijay, M. Metcalfe, E. Boaknin, L. Frunzio, R. J. Schoelkopf, and M. H. Devoret, Dispersive measurements of superconducting qubit coherence with a fast latching readout, Phys. Rev. B **73**, 054510 (2006).

[24] N. Boulant, G. Ithier, P. Meeson, F. Nguyen, D. Vion, D. Esteve, I. Siddiqi, R. Vijay, C. Rigetti, F. Pierre, and M. Devoret, Quantum nondemolition readout using a Josephson bifurcation amplifier, Phys. Rev. B **76**, 014525 (2007).

[25] A. Dewes, F. R. Ong, V. Schmitt, R. Lauro, N. Boulant, P. Bertet, D. Vion, and D. Esteve, Characterization of a Two-Transmon Processor with Individual Single-Shot Qubit Readout, Phys. Rev. Lett. **108**, 057002 (2012).

[26] A. Eddins, J. M. Kreikebaum, D. M. Toyli, E. M. Levenson-Falk, A. Dove, W. P. Livingston, B. A. Levitan, L. C. G. Govia, A. A. Clerk, and I. Siddiqi, High-Efficiency Measurement of an Artificial Atom Embedded in a Parametric Amplifier, Phys. Rev. X **9**, 011004 (2019).

[27] E. I. Rosenthal, C. M. F. Schneider, M. Malnou, Z. Zhao, F. Leditzky, B. J. Chapman, W. Wustmann, X. Ma, D. A. Palken, M. F. Zanner, L. R. Vale, G. C. Hilton, J. Gao, G. Smith, G. Kirchmair, and K. W. Lehnert, Efficient and Low-Backaction Quantum Measurement Using a Chip-Scale Detector, Phys. Rev. Lett. **126**, 090503 (2021).

[28] F. R. Ong, M. Boissonneault, F. Mallet, A. Palacios-Laloy, A. Dewes, A. C. Doherty, A. Blais, P. Bertet, D. Vion, and D. Esteve, Circuit QED with a Nonlinear Resonator: AC-Stark Shift and Dephasing, Phys. Rev. Lett. **106**, 167002 (2011).

[29] F. R. Ong, M. Boissonneault, F. Mallet, A. C. Doherty, A. Blais, D. Vion, D. Esteve, and P. Bertet, Quantum Heating of a Nonlinear Resonator Probed by a Superconducting Qubit, Phys. Rev. Lett. **110**, 047001 (2013).

[30] H. Nakano, S. Saito, K. Semba, and H. Takayanagi, Quantum Time Evolution in a Qubit Readout Process with a Josephson Bifurcation Amplifier, Phys. Rev. Lett. **102**, 257003 (2009).

[31] C. Laflamme and A. A. Clerk, Weak Qubit Measurement with a Nonlinear Cavity: Beyond Perturbation Theory, Phys. Rev. Lett. **109**, 123602 (2012).

[32] M. Boissonneault, A. C. Doherty, F. R. Ong, P. Bertet, D. Vion, D. Esteve, and A. Blais, Back-action of a driven nonlinear resonator on a superconducting qubit, Phys. Rev. A **85**, 022305 (2012).

[33] J. Claudon, A. Zazunov, F. W. J. Hekking, and O. Buisson, Rabi-like oscillations of an anharmonic oscillator: Classical versus quantum interpretation, Phys. Rev. B **78**, 184503 (2008).

[34] P. R. Muppalla, O. Gargiulo, S. I. Mirzaei, B. P. Venkatesh, M. L. Juan, L. Grünhaupt, I. M. Pop, and G. Kirchmair, Bistability in a mesoscopic Josephson junction array resonator, Phys. Rev. B **97**, 024518 (2018).

[35] C. K. Andersen, A. Kamal, N. A. Masluk, I. M. Pop, A. Blais, and M. H. Devoret, Quantum versus classical switching dynamics of driven dissipative Kerr resonators, Phys. Rev. Appl. **13**, 044017 (2020).

[36] D. Sarchi, I. Carusotto, M. Wouters, and V. Savona, Coherent dynamics and parametric instabilities of microcavity polaritons in double-well systems, Phys. Rev. B **77**, 125324 (2008).

[37] C. Eichler, Y. Salathe, J. Mlynek, S. Schmidt, and A. Wallraff, Quantum-Limited Amplification and Entanglement in Coupled Nonlinear Resonators, Phys. Rev. Lett. **113**, 110502 (2014).

[38] P. Winkel, I. Takmakov, D. Rieger, L. Planat, W. Hasch-Guichard, L. Grünhaupt, N. Maleeva, F. Foroughi, F. Henriques, K. Borisov, J. Ferrero, A. V. Ustinov, W. Wernsdorfer, N. Roch, and I. M. Pop, Nondegenerate parametric amplifiers based on dispersion-engineered Josephson-junction arrays, Phys. Rev. Appl. **13**, 024015 (2020).

[39] M. Fischer, Q.-M. Chen, C. Besson, P. Eder, J. Goetz, S. Pogorzalek, M. Renger, E. Xie, M. J. Hartmann, K. G. Fedorov, A. Marx, F. Deppe, and R. Gross, In situ tunable nonlinearity and competing signal paths in coupled superconducting resonators, Phys. Rev. B **103**, 094515 (2021).

[40] M. H. Ansari, Superconducting qubits beyond the dispersive regime, Phys. Rev. B **100**, 024509 (2019).

[41] M. D. Reed, L. DiCarlo, B. R. Johnson, L. Sun, D. I. Schuster, L. Frunzio, and R. J. Schoelkopf, High-Fidelity Readout in Circuit Quantum Electrodynamics Using the Jaynes-Cummings Nonlinearity, Phys. Rev. Lett. **105**, 173601 (2010).

[42] D. Gusenkova, M. Spiecker, R. Gebauer, M. Willsch, D. Willsch, F. Valenti, N. Karcher, L. Grünhaupt, I. Takmakov, P. Winkel, D. Rieger, A. V. Ustinov, N. Roch, W. Wernsdorfer, K. Michielsen, O. Sander, and I. M. Pop, Quantum nondemolition dispersive readout of a superconducting artificial atom using large photon numbers, Phys. Rev. Appl. **15**, 064030 (2021).

[43] V. Schmitt, X. Zhou, K. Juliusson, B. Royer, A. Blais, P. Bertet, D. Vion, and D. Esteve, Multiplexed readout of transmon qubits with Josephson bifurcation amplifiers, Phys. Rev. A **90**, 062333 (2014).

[44] P. Krantz, A. Bengtsson, M. Simoen, S. Gustavsson, V. Shumeiko, W. D. Oliver, C. M. Wilson, P. Delsing, and J. Bylander, Single-shot read-out of a superconducting qubit using a Josephson parametric oscillator, Nat. Commun. **7**, 11417 (2016).

[45] S. S. Elder, C. S. Wang, P. Reinhold, C. T. Hann, K. S. Chou, B. J. Lester, S. Rosenblum, L. Frunzio, L. Jiang, and R. J. Schoelkopf, High-Fidelity Measurement of Qubits Encoded in Multilevel Superconducting Circuits, Phys. Rev. X **10**, 011001 (2020).

[46] L. Chen, *et al.*, Transmon qubit readout fidelity at the threshold for quantum error correction without a quantum-limited amplifier, npj Quantum Inf. **9**, 26 (2023).

[47] K. Rudinger, G. J. Ribeill, L. C. Govia, M. Ware, E. Nielsen, K. Young, T. A. Ohki, R. Blume-Kohout, and T. Proctor, Characterizing midcircuit measurements on a superconducting qubit using gate set tomography, Phys. Rev. Appl. **17**, 014014 (2022).

[48] J. Heinsoo, C. K. Andersen, A. Remm, S. Krinner, T. Walter, Y. Salathé, S. Gasparinetti, J.-C. Besse, A. Potočnik, A. Wallraff, and C. Eichler, Rapid high-fidelity multiplexed readout of superconducting qubits, Phys. Rev. Appl. **10**, 034040 (2018).

[49] S. Krinner, N. Lacroix, A. Remm, A. Di Paolo, E. Genois, C. Leroux, C. Hellings, S. Lazar, F. Swiadek, J. Herrmann, G. J. Norris, C. K. Andersen, M. Müller, A. Blais, C. Eichler, and A. Wallraff, Realizing repeated quantum error correction in a distance-three surface code, Nature **605**, 669 (2022).

[50] N. Sundaresan, T. J. Yoder, Y. Kim, M. Li, E. H. Chen, G. Harper, T. Thorbeck, A. W. Cross, A. D. Córcoles, and M. Takita, Demonstrating multi-round subsystem quantum error correction using matching and maximum likelihood decoders, Nat. Commun. **14**, 2852 (2023).

[51] R. Acharya, *et al.*, Google Quantum AI, Suppressing quantum errors by scaling a surface code logical qubit, Nature **614**, 676 (2023).

[52] D. Sank, *et al.*, Measurement-Induced State Transitions in a Superconducting Qubit: Beyond the Rotating Wave Approximation, Phys. Rev. Lett. **117**, 190503 (2016).